

Get an Unparalleled View of Cellular Diversity
With TotalSeq™ Antibody Cocktails



Learn more ▶



Loss of Mitochondrial Protease CLPP Activates Type I IFN Responses through the Mitochondrial DNA–cGAS–STING Signaling Axis

This information is current as
of June 1, 2022.

Sylvia Torres-Odio, Yuanjiu Lei, Suzana Gispert, Antonia
Maletzko, Jana Key, Saeed S. Menissy, Ilka Wittig, Georg
Auburger and A. Phillip West

J Immunol published online 17 March 2021
<http://www.jimmunol.org/content/early/2021/03/16/jimmunol.2001016>

Supplementary Material <http://www.jimmunol.org/content/suppl/2021/03/16/jimmunol.2001016.DCSupplemental>

Why *The JI*? [Submit online.](#)

- **Rapid Reviews! 30 days*** from submission to initial decision
- **No Triage!** Every submission reviewed by practicing scientists
- **Fast Publication!** 4 weeks from acceptance to publication

**average*

Subscription Information about subscribing to *The Journal of Immunology* is online at:
<http://jimmunol.org/subscription>

Permissions Submit copyright permission requests at:
<http://www.aai.org/About/Publications/JI/copyright.html>

Email Alerts Receive free email-alerts when new articles cite this article. Sign up at:
<http://jimmunol.org/alerts>

The Journal of Immunology is published twice each month by
The American Association of Immunologists, Inc.,
1451 Rockville Pike, Suite 650, Rockville, MD 20852
Copyright © 2021 by The American Association of
Immunologists, Inc. All rights reserved.
Print ISSN: 0022-1767 Online ISSN: 1550-6606.



Loss of Mitochondrial Protease CLPP Activates Type I IFN Responses through the Mitochondrial DNA–cGAS–STING Signaling Axis

Sylvia Torres-Odio,* Yuanjiu Lei,* Suzana Gispert,[†] Antonia Maletzko,[†] Jana Key,[†] Saeed S. Menissy,* Ilka Wittig,[‡] Georg Auburger,[†] and A. Phillip West*

Caseinolytic mitochondrial matrix peptidase proteolytic subunit (CLPP) is a serine protease that degrades damaged or misfolded mitochondrial proteins. CLPP-null mice exhibit growth retardation, deafness, and sterility, resembling human Perrault syndrome, but also display immune system alterations. However, the molecular mechanisms and signaling pathways underlying immunological changes in CLPP-null mice remain unclear. In this study, we report the steady-state activation of type I IFN signaling and antiviral gene expression in CLPP-deficient cells and tissues, resulting in marked resistance to RNA and DNA virus infection. Depletion of the cyclic GMP-AMP (cGAS)–stimulator of IFN genes (STING) DNA sensing pathway reduces steady-state IFN-I signaling and abrogates the broad antiviral phenotype of CLPP-null cells. Moreover, we report that CLPP deficiency leads to mitochondrial DNA (mtDNA) instability and packaging alterations. Pharmacological and genetic approaches to deplete mtDNA or inhibit cytosolic release markedly reduce antiviral gene expression, implicating mtDNA stress as the driver of IFN-I signaling in CLPP-null mice. Our work places the cGAS–STING–IFN-I innate immune pathway downstream of CLPP and may have implications for understanding Perrault syndrome and other human diseases involving CLPP dysregulation. *The Journal of Immunology*, 2021, 206: 000–000.

Mitochondrial proteases are key modulators of several mitochondrial functions, including the maturation of proteins, maintenance of protein quality control, control of mitochondrial gene expression and biogenesis, mitophagy, and apoptosis (1). Caseinolytic mitochondrial matrix peptidase proteolytic subunit (CLPP) is a highly conserved, processive serine

protease located in the mitochondrial matrix. CLPP is the protease component of the caseinolytic peptidase XP (CLPXP) complex that cleaves peptides and various proteins in an ATP-dependent process, together with chaperone and ATPase CLPX (2). Although prokaryotic ClpXP has been extensively studied, the role and function of CLPXP in mitochondria remain less clear, and there is limited information regarding its specific substrates (3). Studies in *Caenorhabditis elegans* have implicated CLPXP as a key component of the mitochondrial unfolded protein response (UPR^{mt}), and downstream signaling and transcriptional responses of the UPR^{mt} are attenuated in worms lacking CLPP activity (4, 5). Mammalian CLPP is involved in pleiotropic cellular functions such as myoblast differentiation, cell proliferation, and mitoribosome assembly, which controls the rate of mitochondrial protein synthesis (6, 7). Moreover, CLPP has recently been implicated in cancer, and hyperactivating CLPP was shown to alter mitochondrial function and selectively kill some cancer cells (8). Thus, drugs targeting CLPP are new candidates for cancer therapy (9).

Studies performed in CLPP-null mice (CLPP-knockout [KO]) highlight the physiological and pathological relevance of this model to the human disorder known as Perrault syndrome (PS). CLPP-KO mice display profound phenotypic changes characterized by growth retardation, deafness, and premature sterility, despite exhibiting only mild mitochondrial bioenergetic deficits (10). Similar phenotypes are also observed in PS, in which the genetic component involves autosomal recessive mutations in CLPP and other nuclear DNA-encoded mitochondrial proteins (11). Other phenotypes of this mouse include insulin resistance and protection from diet-induced obesity (12), accelerated depletion of ovarian follicular reserve (13), and impairment of adaptive thermogenesis due to a decline in brown adipocytes (14).

Eukaryotic mitochondria maintain prokaryotic features, including a circular dsDNA genome, inner membrane cardiolipin, and *N*-formylated proteins, which act as potent triggers of innate immune sensors when released from mitochondria into the cytosol or

*Department of Microbial Pathogenesis and Immunology, College of Medicine, Texas A&M University Health Science Center, Bryan, TX 77807; [†]Experimental Neurology, Goethe University, 60590 Frankfurt am Main, Germany; and [‡]Functional Proteomics, Faculty of Medicine, Goethe University, 60590 Frankfurt am Main, Germany
ORCID: 0000-0002-7486-4261 (Y.L.); 0000-0003-2884-6895 (A.P.W.).

Received for publication September 4, 2020. Accepted for publication February 1, 2021.

This work was supported by Office of the Assistant Secretary of Defense for Health Affairs, U.S. Department of Defense Awards W81XWH-17-1-0052 and W81XWH-20-1-0150 (to A.P.W.) through the Peer Reviewed Medical Research Programs. Additional support was provided by National Heart, Lung, and Blood Institute, National Institutes of Health (NIH) Grant R01HL148153 (to A.P.W.). Opinions, interpretations, conclusions, and recommendations are those of the authors and are not necessarily endorsed by the NIH or the U.S. Department of Defense.

The proteomics data presented in this article have been submitted to the ProteomeXchange Consortium (<http://proteomecentral.proteomexchange.org>) under accession number PXD023677.

Address correspondence and reprint requests to Dr. A. Phillip West, Texas A&M Health Science Center, 8447 Riverside Parkway, MREB 1 3012, Bryan, TX 77807. E-mail address: awest@tamu.edu

The online version of this article contains supplemental material.

Abbreviations used in this article: CAM, chloramphenicol; CLPP, caseinolytic mitochondrial matrix peptidase proteolytic subunit; CLPXP, caseinolytic peptidase XP; DAMP, damage-associated molecular pattern; ddC, dideoxycytidine; Drp1, dynamin-related protein 1; hpi, hour postinfection; IDT, Integrated DNA Technologies; IFNAR, IFN α/β receptor; ISG, IFN-stimulated gene; KO, knockout; MEF, mouse embryonic fibroblast; Mfn1, mitofusin 1; MOI, multiplicity of infection; mtDNA, mitochondrial DNA; PS, Perrault syndrome; siRNA, small interfering RNA; TFAM, transcription factor A mitochondrial; UPR^{mt}, mitochondrial unfolded protein response; VDAC, voltage-dependent anion channel; VSV, vesicular stomatitis virus; WT, wild-type.

Copyright © 2021 by The American Association of Immunologists, Inc. 0022-1767/21/\$37.50

extracellular space. The release and accumulation of these so-called mitochondrial damage-associated molecular patterns (DAMPs) are increasingly implicated in the inflammatory pathology of human disorders, including autoimmunity, neurodegenerative diseases, and cancer (15–17). Our prior work identified antiviral gene signatures in CLPP-KO mice consistent with steady-state activation of innate immunity (10, 18). However, the mitochondrial molecular mechanisms and innate immune signaling pathways underlying activation of antiviral signatures in CLPP-KO mice remain uncharacterized, and the biological significance of this phenotype is unclear.

In this study, we show that enhanced antiviral gene expression in CLPP-KO mice is triggered by mitochondrial DNA (mtDNA) release and mediated by the cGAS–STING DNA sensing pathway. Deletion of STING or the IFN α/β receptor (IFNAR) in CLPP-KO mouse embryonic fibroblasts (MEFs) ablates steady-state expression of broadly antiviral IFN-stimulated genes (ISGs) and reduces the potent antiviral phenotypes observed during RNA and DNA virus infection. These findings shed light on a new mitochondrial pathway upstream of cGAS and STING, link mitochondrial proteostasis to mtDNA genome maintenance, and may have important implications for understanding mitochondrial-innate immune cross-talk in the context of human health and disease.

Materials and Methods

Mouse strains

Embryonal stem cell line IST13563G11 (line G), with heterozygous GeneTrap insertions at *Clpp* intron 2, was rederived at the Texas Institute for Genomic Medicine on a C57BL/6N background. Heterozygous breeders were mated to generate *Clpp*-null (CLPP-KO) mutant and littermate wild-type (WT) control offspring. *Sting*^{gt/gt} (C57BL/6J-*Sting*^{1st/J}, strain 017537) and *Ifnar*^{-/-} (B6(Cg)-*Ifnar*^{tm1.2Ees/J}, strain 028288) were obtained from The Jackson Laboratory. CLPP heterozygous mutant mice were crossed with *Sting*^{gt/gt} and *Ifnar*^{-/-} for several generations to obtain double-KO mice on a C57BL/6NJ mixed background. All animal experiments were conducted in compliance with the guidelines established by the Texas A&M University Institutional Animal Care and Use Committee.

Cell culture

Primary WT, CLPP-KO, STING^{gt/gt}, IFNAR^{-/-} (IFNAR-KO), CLPP-KO/STING^{gt/gt}, and CLPP-KO/IFNAR-KO MEFs were generated from E12.5 to 14.5 embryos. Cells were maintained in DMEM (D5756-500ML; Sigma-Aldrich) supplemented with 10% FBS (VWR International) and subcultured for no more than five passages before experiments. Transfection of MEFs with small interfering RNA (siRNA) was performed with Lipofectamine RNAiMax (13778-150; Invitrogen) in Opti-MEM media (11058021; Thermo Fisher Scientific), and the following siRNAs were used at a final concentration of 25 nM: small interfering cGAS (MMC.RNAL.N173386.12.1; Integrated DNA Technologies [IDT]), siRNA mPolg2 (NM_015810; Sigma-Aldrich), small interfering mitofusin 1 (Mfn1) (NM_024200; Sigma-Aldrich), small interfering dynamin-related protein 1 (Drp1) (MMC.RNAL.N152816.12.1), small interfering CpX (MMC.RNAL.N011802.12.2 IDT), and siRNA Negative Control Dicer-Substrate Short Interfering RNA) 51-01-14-03; IDT) according to manufacturer's instructions. Cells were harvested for RNA or protein between 48 and 72 h later. For Rig-I/MDA5 challenge, cells were transfected with Poly(I:C) (P1530; Sigma-Aldrich) complexed in polyethylenimine (43896; Alfa Aesar) in Opti-MEM media. For LPS, cells were treated with LPS (LPS-B5 Ultrapure, tlr1-pb5lps; InvivoGen) at 1 $\mu\text{g}/\text{ml}$ and harvested for RNA 4 h later. For mtDNA depletion, dideoxycytidine (ddC) (D5782; Sigma-Aldrich) was resuspended in PBS, added to MEFs at a final concentration of 150 μM , and refreshed every 48 h for 4 d. For chloramphenicol (CAM) treatment, cells were treated with CAM (R4408; Sigma-Aldrich) at different concentrations (50–200 μM) and harvested for protein between 24 and 48 h later. For VBIT-4 treatment, VBIT-4 (HY-129122; MedChem Express) was resuspended in DMSO at 10 mM and added to the media at a final concentration of 10 μM for 48 h, whereas control cells were treated with DMSO. For VBIT-4 treatment plus challenge, cells were treated with VBIT-4 and 6 h before the 48 h harvesting time, mouse IFN β (8234-MB-010/CF; R&D Systems) was added to the cells at a final concentration of 1 ng/ml. All cells were harvested 48 h after challenge for RNA analysis. To generate CLPP

knockdown human foreskin fibroblasts (HFF-1), MISSION short hairpin RNA (shRNA) Lentiviral Transduction Particles against human CLPP (TRCN0000291174), or eGFP (RHS4459) were purchased from Sigma-Aldrich and Horizon Discovery, respectively. HFF-1 were transduced with the shRNA encoding lentivirus stocks in the presence of polybrene (8 $\mu\text{g}/\text{ml}$) and stably selected with puromycin.

Viral stocks and infections

Vesicular stomatitis virus (VSV)-G/GFP and HSV1/GFP were maintained as described previously (19, 20). MEFs were plated in 12-well plates at 7×10^4 cells per well 16 h before infection in DMEM + 10% FBS. The next morning, virus stocks were diluted at indicated multiplicity of infections (MOIs) in serum-free DMEM (D5756-500ML; Sigma-Aldrich). Three hundred microliters serum-free media containing virus (or DMEM alone for the control wells) was gently added to wells. Plates were incubated at 37°C 5% CO₂ and rocked gently every 15 min for 1 h, after which the supernatant was removed, bleached, and discarded. Then, 0.5 ml of fresh DMEM + 10% FBS was added to each well, and the cells were allowed to incubate for the duration of the experiment. At the indicated times postinfection, supernatant was collected and cleared by centrifugation at 6000 rpm, 4°C, then kept at -80°C until further processing. Cells were then fixed and stained for microscopy or lysed in RNA Lysis Buffer. For plaque assay, BHK-1 or Vero cells were plated in six-well plates at 95% confluency in 3% methylcellulose containing DMEM media. Next, different dilutions of supernatant from VSV- or HSV1-infected MEFs were added to the cells and incubated until plaques were visible between 24 and 72 h. Plaques were stained with Cresyl Violet and counted with ImageJ software.

Immunofluorescence microscopy

Cells were grown on 12- or 18-mm coverslips and treated or infected as described. After washing in PBS, cells were fixed with 4% paraformaldehyde for 20 min, permeabilized with 0.1% Triton X-100 in PBS for 5 min, blocked with PBS containing 10% FBS for 30 min, stained with primary Abs for 60 min, and stained with secondary Abs for 60 min. Cells were washed with PBS between each step. Coverslips were mounted with ProLong Gold Antifade reagent containing DAPI (Molecular Probes). For viral infections, viral GFP fluorescence images were captured using the LionHeart FX fluorescent microscope at original magnification $\times 20$ and tiling images at 2×2 . For mtDNA nucleoid staining, an original magnification $\times 60$ oil-immersed objective was used, and images were taken with a Confocal Laser Scanning Microscope (Olympus FV3000). Images were processed in ImageJ software. Nucleoid area quantification was performed largely as described (21). Briefly, approximately six to eight unique fields of view from five distinct confocal images (of each genotype at each treatment) comprising between 200 and 400 nucleoids, were captured at random. After incorporating scale information obtained from the FV3000 software, images were made binary, and the area of each nucleoid was determined using the “Analyze Particles” feature of ImageJ. Nucleoids were binned into the three size cutoffs ($<200 \text{ nm}^2$, between 200 and 450 nm^2 , and $>450 \text{ nm}^2$), and the percentage of nucleoids falling within each category was plotted.

Quantitative PCR

To measure relative gene expression by quantitative RT-PCR, total cellular RNA was isolated using the Quick-RNA Micro Prep Kit (R1051; Zymo Research). Approximately 250–500 ng RNA was normalized across samples, and cDNA was generated using the qScript cDNA Synthesis Kit (101414-098; VWR International). cDNA was then subjected to quantitative PCR using PerfeCTa SYBR Green FastMix (84069; Quantabio) and primers as indicated in Table I. Three technical replicates were performed for each biological sample, and expression values of each replicate were normalized against Rp137 using the $2^{-\Delta\Delta C_t}$ method. For relative expression (fold), control samples were centered at one; for relative expression (in percentage), control samples were centered at 100%. mtDNA extraction and abundance analysis was performed as described (21) using primers specific to mtDNA regions and normalized against nuclear Telomerase (Tert) DNA.

Proteomics

CLPP-KO MEF and their matching controls ($n = 3$) were analyzed by quantitative mass spectrometry essentially as described in Ref. 22. Mass spectrometry data were analyzed by MaxQuant (1.5.3.30) (23) using a mouse proteome Uniprot database (Download 2/2016) and a false discovery rate $<1\%$. For quantification, proteins were quality filtered according to a minimum of three valid values in one group ($n = 3$) using

Perseus software (v. 1.5.2.6). All missing values from this reduced matrix were replaced by background value from normal distribution. For statistical comparison, Student *t* test were used. The mass spectrometry proteomics data have been deposited to the ProteomeXchange Consortium (<http://proteomecentral.proteomexchange.org>) via the PRIDE partner repository with the dataset identifier PXD023677.

Subcellular fractionation

Cellular fractionation was performed largely as described (24). In brief, cells were divided into two aliquots, and one aliquot (10%) was resuspended in 50 μ l of 1% SDS lysis buffer, boiled for 5 min, sonicated for 1 min, and saved as whole-cell lysate. The second equal aliquot (90%) was resuspended in 400 μ l extraction buffer containing 10 mM HEPES, 10 mM KCl, 1.5 mM MgCl₂, 0.34 M sucrose, 10% glycerol, 0.2% NP-40 (pH 7–7.6), and protease inhibitors. The homogenates were incubated on ice for 10 min with occasional vortexing, centrifuged at 6500 \times *g* for 5 min three times, and the supernatant was saved as the postnuclear fraction. The nuclei were then washed for 1 min on ice in extraction buffer and centrifuged at 6500 \times *g* for 5 min at 4°C twice, resuspended in 150 μ l of 1% SDS lysis buffer, boiled at 95°C for 5 min, and sonicated for 1 min. After a high-speed 20,000 \times *g* spin to pellet sheared DNA, the supernatant was saved as the nuclear fraction.

Immunoblotting

Proteins from either homogenized tissue (<50 mg) or cells (<1 \times 10⁷) were lysed in 1% NP-40 buffer and spun down at 15,000 rpm for 10 min at 4°C. The supernatant was collected as protein lysate and quantified with micro-BCA assay (23235; Proteintech). Between 20 and 30 μ g of protein was separated on 10–20% polyacrylamide gradient gels, then transferred onto PVDF membranes at 100 V for 1 h. Membranes were dried for 30 min and incubated with primary Abs (Table II) overnight at 4°C. Membranes were washed with 1 \times PBS for 30 min and incubated with HRP-conjugated secondary Abs for 1 h. Membranes were washed with PBS for 1 h before developing with Millipore Luminata Crescendo HRP Substrate (WBWR0500).

EchoMRI

Body composition analysis on live mice was completed using the EchoMRI-100H at the Rodent Preclinical Phenotyping Core at Texas A&M University. This analyzer delivers precise body composition measurements of fat, lean, free water, and total water masses in live animals weighing up to 100 g.

Statistical analyses

Error bars displayed throughout the manuscript represent the mean \pm SEM unless otherwise indicated and were calculated from triplicate or quadruplicate technical replicates of each biological sample. Sample sizes were chosen by standard methods to ensure adequate power, and no randomization or blinding was used for animal studies. No statistical method was used to predetermine sample size. Statistical analysis was determined using GraphPad software, and statistics tests include unpaired Student *t* test, ordinary one-way ANOVA, and two-way ANOVA with Tukey post hoc. Significance was established as **p* < 0.05, ***p* < 0.01, ****p* < 0.001, and *****p* < 0.0001 or NS when *p* > 0.05. Data shown are representative of two to three independent experiments (unless otherwise specified), including microscopy images, Western blots, and viral challenges.

Results

CLPP deficiency leads to steady-state ISG expression and an antiviral signature in cells and tissues

We first expanded upon our prior findings that revealed increased steady-state expression of antiviral genes in CLPP-deficient tissues (10). Using Ingenuity Pathway Analysis software, we observed that predicted upstream regulators of the antiviral gene signature in CLPP-KO tissues included factors governing IFN-I signaling (*Irf7*, *Irf3*, and *Stat1*), IFN- α , and IFNAR (Supplemental Fig. 1A). Among the list of upregulated IRF7 and STAT1 target genes, we identified canonical ISGs such as *Usp18*, *Ifit1b*, *Ifi44*, and *Rtp4* (Supplemental Fig. 1B). Individual analyses of heart and liver tissues from 3- to 5-mo-old mice revealed a significant enhancement of ISGs at the protein level in both the liver and heart of CLPP-KO mice (Supplemental Fig. 1C, 1D).

To better characterize this ISG response, we used MEFs and human foreskin fibroblasts deficient in CLPP. Expression profiles of CLPP-KO MEFs revealed an enrichment of ISGs and antiviral signaling factors at both the RNA (Table I) and protein (Table II) level (Fig. 1A–C). Among the set of overexpressed ISGs, we observed those involved in direct antiviral activity (VIPERIN/Rsad2, IFIT1, and IFIT3); regulators of antiviral and IFN-I signaling (USP18, STAT1, and STAT2); and RNA and DNA sensors (RIG-I, MDA5, and ZBP1). Global proteome profiling revealed that >60% of the most differentially expressed proteins in CLPP-KO MEFs were ISGs (Fig. 1C). Consistent with enhanced IFN-I responses and ISG expression, CLPP-KO MEFs showed elevated levels of transcription factors IRF7, STAT1, and STAT2 in whole-cell and nuclear fractions compared with WT cells (Fig. 1D). Similarly, CLPP-KO cells showed higher transcript levels of *Ifnb1*, but no significant differences in IFN- α gene expression (*Ifna1*, *Ifn14*, and *Ifna5*) (Fig. 1E).

Transfection of CLPP-KO MEFs with poly(I:C), a dsRNA analogue agonist of the cytosolic RNA helicase MDA5, or challenge with LPS, a TLR4 ligand, revealed elevated ISG expression compared with WT, which indicated potentiation/priming of antiviral signaling pathways downstream of both cytosolic and membrane-bound pattern-recognition receptors (Fig. 1F). To assess if this heightened ISG response was also observed in human cells, we transduced human foreskin fibroblasts with shRNAs targeting CLPP or EGFP as a control. Similar to our findings in MEFs and murine tissues, reduction of CLPP in human fibroblasts led to the steady-state upregulation of antiviral ISGs at the protein level, including IFIT2, IFITM1, RIG-I, STAT1, and others (Fig. 1G).

STING and IFNAR mediate the steady-state ISG and antiviral signature observed in CLPP-deficient cells and tissues

Recent work has revealed that the release of mitochondrial nucleic acid DAMPs into the cytosol is a potent trigger of DNA and RNA sensors of the innate immune system (21, 25, 26). To next pinpoint downstream sensors mediating the antiviral response in CLPP-KO cells, we transiently knocked down the DNA sensor cGAS or the cytosolic RNA adaptor MAVS and quantified ISG responses in MEFs. Downregulation of cGAS profoundly diminished the ISG response in CLPP-KO MEFs (Fig. 2A), whereas MAVS depletion did not (Supplemental Fig. 2A), implicating the cytosolic DNA sensing machinery as the main trigger of ISGs in CLPP-deficient cells. Using a parallel approach to bypass any off-target and immune stimulatory effects of transient siRNA transfection, we crossed CLPP heterozygous mutant mice with *Sting*^{gt/gt} and *Ifnar*^{-/-} strains to generate CLPP-KO/STING^{gt/gt} and CLPP-KO/IFNAR-KO mice, respectively, and assessed the antiviral response in MEFs and tissues. Consistent with our siRNA data implicating the cGAS pathway, the relative expression of ISGs *Usp18*, *Isg15*, and *Cxcl10* was markedly reduced in the absence of STING (Fig. 2B), with this effect being more pronounced in CLPP-KO/IFNAR-KO MEFs. Ablation of elevated IFN-I signaling was also observed in RNA extracts from tissues of the double-mutant crosses, as quantitative RT-PCR analysis of heart (Fig. 2C) and liver (Supplemental Fig. 2B) showed diminished ISG expression in double-KO mice compared with CLPP-KO alone. A similar effect was observed in antiviral proteins such as RIG-I, STAT1, ZBP1, and IFIT3 in heart extracts (Fig. 2D), with marked decreases in all ISGs in CLPP-KO/STING^{gt/gt} and CLPP-KO/IFNAR-KO mice compared with CLPP-KO alone. Although ablation of STING and IFNAR was sufficient to blunt the steady-state ISG signature in CLPP-KO cells and tissues, loss of STING or IFNAR signaling was not sufficient to rescue the growth deficits and small testis size of CLPP-KO mice (Supplemental Fig. 2C) Moreover, STING depletion did not

Table I. Sequences of primers used for quantitative PCR

Gene	Forward and Reverse Primer Sequences	Gene	Forward and Reverse Primer Sequences
<i>Cmpk2</i>	5'-AAAGAATCAACCAACTTT-3' 5'-GGCTCCACTCACCTCAGTA-3'	<i>Rsad2</i>	5'-ATAGTGAATGCGAGGCCT-3' 5'-AACCTGTGATGCAAGCTGT-3'
<i>Cxcl10</i>	5'-CCAAGTGTGCCGTCAATTTTC-3' 5'-GGCTCGCAGGGATGATTTCAA-3'	<i>Rp137</i>	5'-CATCCTTTGGTAAGCGTCGCA-3' 5'-TGGCCTCCAGTTATACTTCCT-3'
<i>Drp1</i>	5'-TCCCAATTCATTATCCTCGC-3' 5'-CATCAGTACCCGCATCCATG-3'	<i>Usp18</i>	5'-GAGAGGACCATGAAGAGGA-3' 5'-TAAACCAACCAGACCATGAG-3'
<i>Ifit1</i>	5'-CAAGCAGGTTTCTGAGGAG-3' 5'-GACCTGGTCACCATCAGCAT-3'	<i>Zbp1</i>	5'-TCAAAGGGTGAAGTCATGGA-3' 5'-GTGGAGTGGCTTCAGAGCTT-3'
<i>Ifit3</i>	5'-TTCCAGCAGCACAGAAAC-3' 5'-AAATTCAGGTGAAATGGCA-3'	ATP6	5'-CCTTCCACAAGGAACCTCAATTTCCAC-3' 5'-CTAGAGTAGCTCCTCCGATTAGGTG-3'
<i>Ifna1</i>	5'-GAGAGAAACACAGCCCTG-3' 5'-TCAGTCTTCCAGCACATTG-3'	CO3	5'-GACGTAATTCGTGAAGGAACCTACC-3' 5'-GATAGAACGCTCAGAAGAATCCTGC-3'
<i>Ifna4</i>	5'-CTTTCCTCATGATCCTGGTAATGAT-3' 5'-AATCCAAAATCCTTCTGCTCTTC-3'	CTYB	5'-GCTTTCACCTTCATCTTACCATTTA-3' 5'-TGTTGGGTTGTTTGTATCCG-3'
<i>Ifna5</i>	5'-GACTCATCTGCTGCATGGAA-3' 5'-TGTTGCATCACACAGGCTTT-3'	DLOOP	5'-AATCTACCATCCTCCGTGAAACC-3' 5'-TCAGTTTACTACCCCAAGTTTAA-3'
<i>Ifnb1</i>	5'-CCCTATGGAGATGACGGAGA-3' 5'-CCCAGTGTGGAGAAATTTG-3'	ND6	5'-TTTAGCATTAAAGACCTTACC-3' 5'-CCAACAACCCTTAACAAT-3'
<i>Irgm1</i>	5'-CCAGGAAGGCCACTAACATC-3' 5'-TGTTCTCTCGAATGCCTTA-3'	TERT	5'-CTAGCTCATGTGTCAAGACCCTCTT-3' 5'-GCCAGCAGTTTCTCTCGTT-3'
<i>Isg15</i>	5'-CTAGAGCTAGAGCCTGCAG-3' 5'-AGTTAGTACACGGACACCAG-3'	HSV1 ICP27 RNA	5'-TTTCTCCAGTGTCTACCTGAAGG-3' 5'-TCAACTCGCAGACGACTCG-3'
<i>Mfn1</i>	5'-ATGGCAGAAACGGTATCTCCA-3' 5'-GCCCTCAGTAACAACTCCAGT-3'	HSV1 UL30 RNA	5'-CGCGCTTGGCCGGGATTAACAT-3' 5'-TGGGTGTCCGGCAGAAATAAGC-3'
<i>Polg2</i>	5'-TGAAATGTGTCTACGATACAGG-3' 5'-GCTGGAAGGAATCGTAGAGGT-3'	VSV-G	5'-CAAGTCAAAATGCCCAAGAGTCACA-3' 5'-TTTCTTGCATTGTTTACAGATGG-3'
<i>Rnf213</i>	5'-TTTGTACCGTTCCCCCAAT-3' 5'-GTTCACTGCCTCCAATTGCT-3'	VSV-M	5'-TATGATCCGAATCAATTAAGATATG-3' 5'-GGGACGTTTCCCTGCCATTCCGATG-3'

significantly impact body composition changes (i.e., fat/lean ratio via EchoMRI) resulting from loss of CLPP (Supplemental Fig. 2D).

CLPP-KO cells are more resistant to viral infection owing to elevated activation of the STING pathway

To next assess if basal cGAS-STING-IFN-I signaling and increased steady-state expression ISGs in CLPP-KO cells is functionally relevant, we infected MEFs with recombinant VSV expressing the viral protein VSV-G fused to GFP (VSV-G/GFP) (19). Postinfection at an MOI of 0.1 for 24 h, microscopic analysis showed a striking absence of GFP fluorescence in CLPP-KO cells compared with WT controls (Fig. 3A). Quantification of GFP (Supplemental

Fig. 3A) indicated that only 1.3% of CLPP-KO cells were positive for GFP compared with 25% of WT cells. STING^{gt/gt} cells were more susceptible to VSV infection consistent with prior results (27, 28), with more than 60% of cells staining GFP positive. Similarly, 68% of CLPP-KO/STING^{gt/gt} cells were GFP positive, indicating that viral resistance of CLPP-KO cells was completely lost in CLPP-KO/STING^{gt/gt} MEFs. Relative levels of viral RNA transcripts for VSV-G and VSV-M were reduced >95% in CLPP-KO cells compared with WTs (Fig. 3B). In contrast, viral transcript levels were equally high in VSV-infected STING^{gt/gt} and CLPP-KO/STING^{gt/gt} cells. Similar results were found at earlier VSV infection timepoints (i.e., 16 h postinfection [hpi], Supplemental Fig. 3B),

Table II. List of Abs and dilutions used

Name	Company	Catalog Number	Dilution
CLPX	Abcam	ab168338 [EP8772]	1:1000
IFIT3	Gift from G. Sen at Cleveland Clinic		1:10,000
ZBP1	AdipoGen	AG-20B-0010	1:1000
STAT1	Cell Signaling Technology	9172S	1:1000
STAT2 (D9J7L)	Cell Signaling Technology	72604	1:1000
cGAS	Cell Signaling Technology	31659	1:1000
RIG-I	Cell Signaling Technology	4200S	1:1000
IRGM1	Cell Signaling Technology	14979	1:1000
MAVS	Cell Signaling Technology	4983	1:1000
IRF7 (D8V1J)	Cell Signaling Technology	72073	1:1000
IRF3 (D83B9)	Cell Signaling Technology	4302	1:1000
αTUBULIN	Developmental Studies Hybridoma Bank	12G10	1:5000
GFP	Developmental Studies Hybridoma Bank	8H11	1:30
TFAM	MilliporeSigma	ABE483	1:1000
Anti-DNA	MilliporeSigma	CBL-186 (AC-30-10)	1:300
IFITM1	Proteintech	60074-1-Ig	1:5000
IFIT2	Proteintech	12604-1	1:1000
Calnexin	Proteintech	10427-2-AP	1:1000
β-Actin	Proteintech	66009-1-Ig	1:5000
CLPP	Proteintech	15698-1	1:1000
GAPDH	Proteintech	60004-1-LG	1:5000
Histone 3	Proteintech	17168-1-AP	1:5000
HSP60	Santa Cruz Biotechnology	sc-1052	1:5000
Cytochrome c oxidase subunit I (COI)	Thermo Fisher Scientific	459600 (ID6E1A8)	1:1000

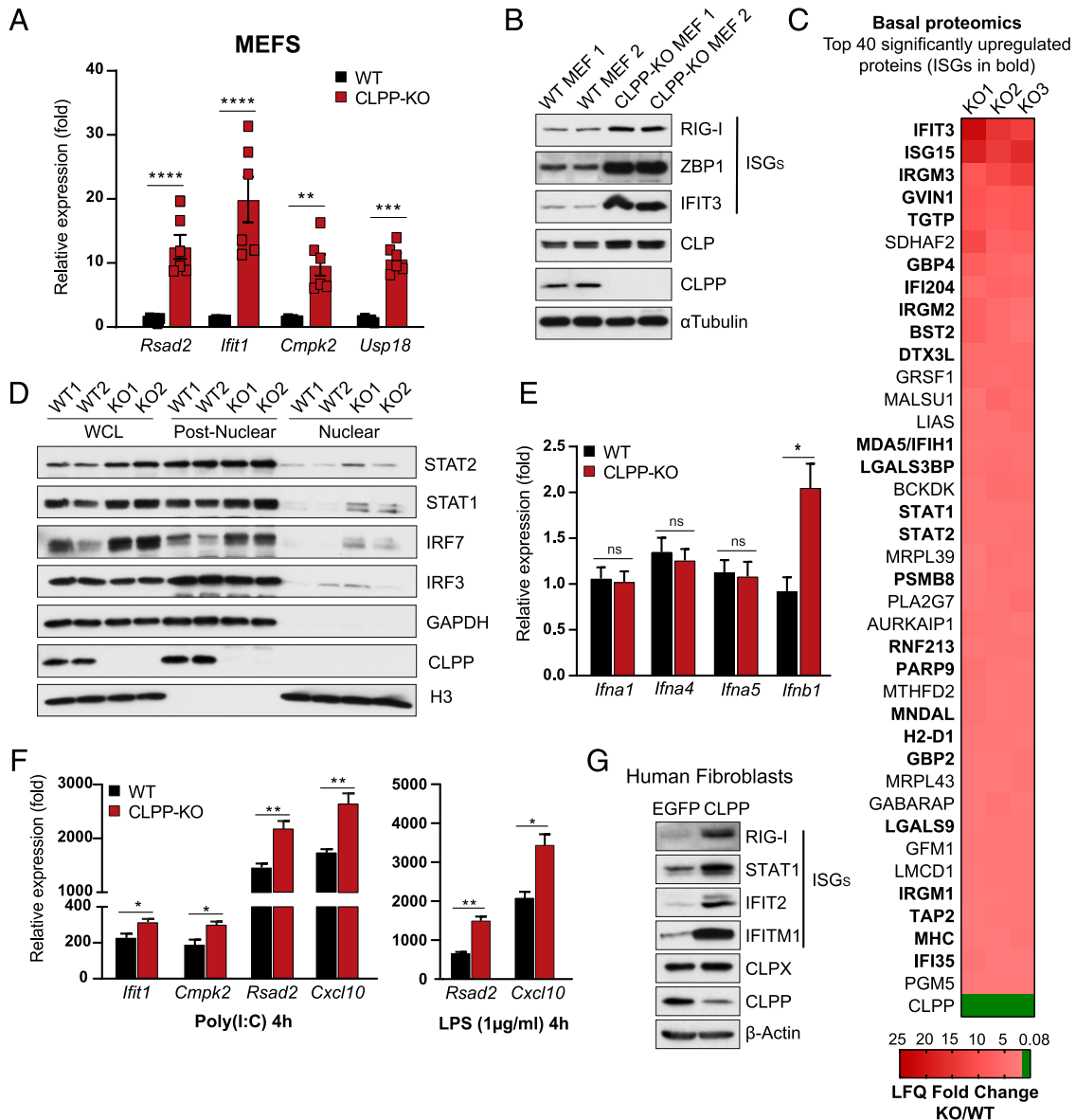


FIGURE 1. CLPP deficiency leads to steady-state ISG expression in mouse and human cells. **(A and B)** Quantitative real-time PCR (A) and Western blots (B) of baseline ISGs of littermate WT and CLPP-KO MEFs lines [$n = 6$ MEF lines per genotype in (A) and two in (B)]. **(C)** Heat map from the top 40 significantly ($p < 0.05$) upregulated proteins from baseline proteomic data of littermate WT and CLPP-KO MEFs. Data represented as label-free quantification (LFQ) fold change of each CLPP-KO MEFs over average WT ($n = 3$ MEF biological replicates). **(D)** Western blotting of baseline transcription factors after subcellular fractionation of WT and CLPP-KO MEFs ($n = 2$ MEF lines). **(E)** Quantitative real-time PCR of type I IFN gene expression in littermate WT and CLPP-KO MEFs ($n = 2$ MEFs lines pooled). **(F)** Quantitative real-time PCR of ISGs in WT and CLPP-KO MEFs, 4 h after transfection with poly(I:C) or LPS challenge ($n = 3$ biological replicates pooled). **(G)** Human foreskin fibroblasts were transduced with the shRNA against CLPP and EGFP (as control) and selected with puromycin (2 $\mu\text{g/ml}$). After selection, cells were plated in 12-well dishes and harvested for Western blots of baseline ISGs. Error bars represent mean \pm SEM, and all figures are representative of three independent experiments. In (A), two-way ANOVA Tukey post hoc, and in (E) and (F), Student t test were used to determine significance. * $p < 0.05$, ** $p < 0.01$, *** $p < 0.001$, **** $p < 0.0001$.

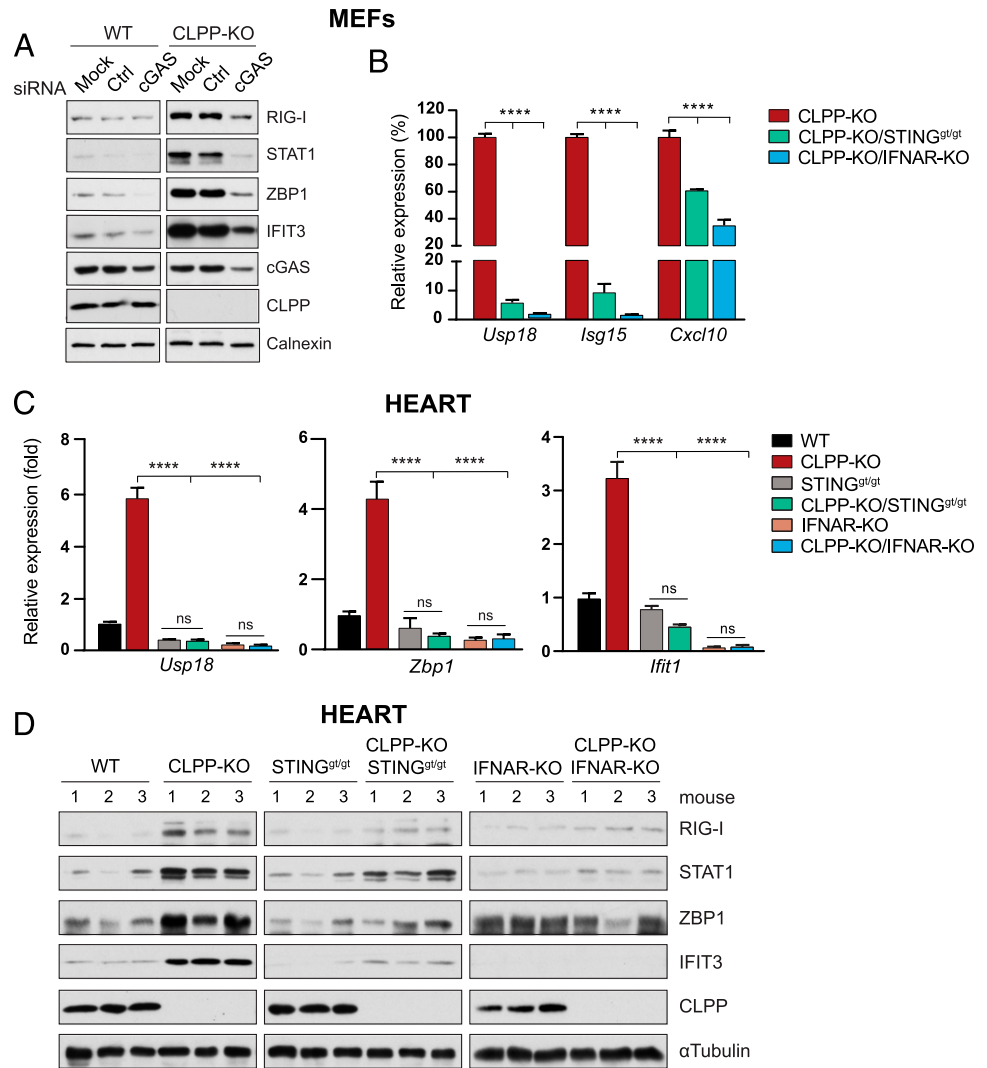
corroborating microscopic results demonstrating that antiviral phenotypes of CLPP-KO cells are mediated by STING signaling.

At 24 hpi, there was a striking reduction of viral plaques in CLPP-KO MEFs (two-log reduction) compared with WT. This contrasted strongly with CLPP-KO/STING^{gt/gt} cells, which exhibited only a small, 1.7-fold reduction compared with STING^{gt/gt} littermate MEFs. The viral protection observed in CLPP-KO cells is likely due to both elevated baseline and induced ISGs, as levels of antiviral genes *Usp18* and *Cmpk2* were further enhanced in CLPP-KO over WT controls after VSV infection (Supplemental Fig. 3C). Although the VSV-mediated upregulation of ISGs in CLPP-KO cells was greatly blunted by loss of STING, the fold induction of ISGs in double-mutant CLPP-KO/STING^{gt/gt} MEFs

over infected STING^{gt/gt} MEFs was similar to CLPP-KO over WT cells. RNA viruses such as VSV predominantly engage the RIG-I–MAVS pathway, and although some reports have noted cross-talk between the MAVS and STING pathways, MAVS signaling remains largely functional in the absence of cGAS and STING (29). Thus, the baseline antiviral priming in CLPP-KO cells driven by persistent STING–IFN-I signaling, and not the potentiated induction of ISGs during infection, is likely the most important factor governing the resistance of CLPP-KO cells to VSV.

To determine if the viral resistance extended to DNA viruses, we infected MEF lines with HSV-1, a dsDNA virus that employs several diverse mechanisms to evade innate antiviral responses. Postinfection at an MOI 0.001 and incubation for 72 h, HSV-1 viral

FIGURE 2. STING and IFNAR mediate the steady-state ISG and antiviral signature in CLPP-deficient cells and tissues. **(A)** Representative Western blots of ISGs in WT and CLPP-KO MEFs transfected with control (Ctrl) or cGAS siRNA for 72 h. Experiment was repeated three times with two MEF lines. **(B)** Quantitative real-time PCR of baseline ISGs in WT, CLPP-KO, and CLPP-KO/STING^{g1/g1} or CLPP-KO/IFNAR-KO double-mutant MEFs. Real-time PCR data were represented as relative expression percentage (%) with CLPP-KO set to 100% ($n = 3$ biological replicates). **(C and D)** Quantitative RT-PCR (C) and Western blots (D) of baseline ISGs from heart tissue from three 12-mo-old male mice per genotype. Error bars represent as mean \pm SEM of triplicates and all figures are representative of three independent experiments. One-way ANOVA Tukey post hoc was used to determine significance. **** $p < 0.0001$. ns, nonsignificant.



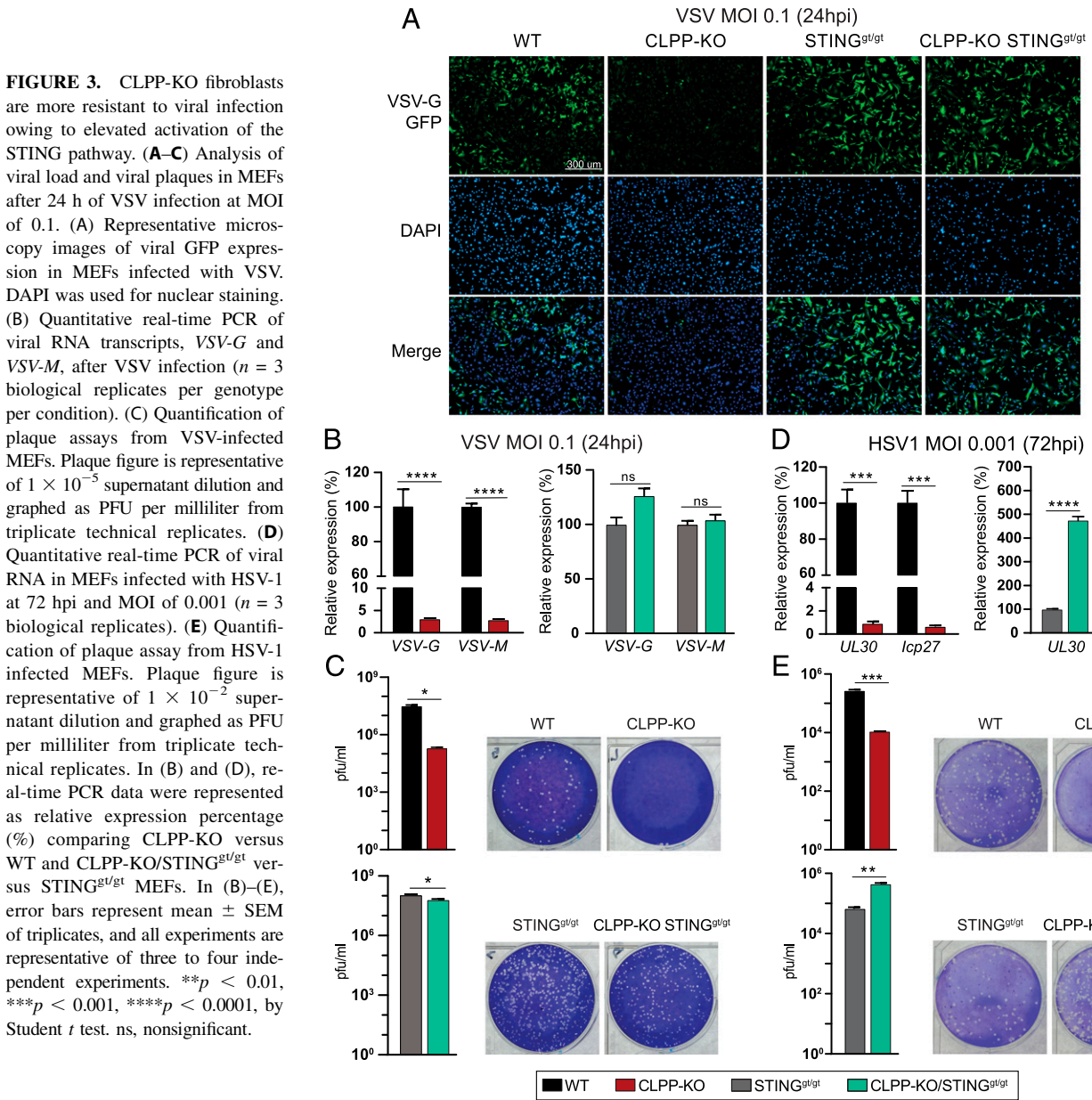
RNAs *UL30* and *Icp27* were reduced >95% in CLPP-KO MEFs compared with WT controls (Fig. 3D), mirroring findings seen with VSV infections. The dramatic reduction in HSV-1 RNA expression in CLPP-KO cells was lost in double-KO cells, and in fact, we observed that CLPP-KO/STING^{g1/g1} MEFs exhibited five times more viral RNA transcripts than STING^{g1/g1} littermates (Fig. 3D). This marked increase in viral RNAs in the double-KO cells was not observed in VSV infections, in which there was only a minor increase in viral transcripts in CLPP-KO/STING^{g1/g1} MEFs over infected STING^{g1/g1} MEFs (Fig. 3C). A similar trend was observed in quantification of viral particles by plaque assays, as we observed resistance of CLPP-KO cells to HSV-1 (1.5-log reduction in plaques) compared with WT cells (Fig. 3E). However, CLPP-KO/STING^{g1/g1} cells were more susceptible to HSV-1 infection (0.5-log increase in plaques) compared with STING^{g1/g1}, consistent with viral RNA expression data.

We next assessed whether the strong antiviral response was maintained at a higher and more lytic MOI, at which HSV-1 virulence and IFN-I-repressive mechanisms are more potent. At an MOI of 0.01 48 hpi, CLPP-KO cells remained more resistant to HSV-1, albeit to a lesser extent compared with infection with a lower MOI (Supplemental Fig. 3D). CLPP-KO cells showed a 40% reduction in *UL30* and *Icp27* expression compared with WTs. However, similar to results from MOI 0.001 infections, CLPP-KO/STING^{g1/g1} MEFs exhibited five times more viral RNA than STING^{g1/g1} cells (Supplemental Fig. 3D). Collectively, these

results show that potentiated cGAS-STING-dependent IFN-I responses in CLPP-deficient cells promote a robust antiviral state that is broadly restrictive to both RNA and DNA viruses.

CLPP deficiency results in altered mtDNA abundance and nucleoid morphology

Our prior work has documented that mtDNA stress and cytosolic release is a potent inducer of IFN-I responses via the cGAS-STING DNA sensing axis (21). Because the ISG and antiviral priming phenotypes in CLPP-KO cells and tissues were dependent on cGAS-STING, we hypothesized that mtDNA might be the mitochondrial DAMP triggering this response. Interestingly, we found that MEFs and tissues (10) from CLPP-KO mice exhibit baseline elevations in mtDNA abundance by quantitative PCR-based approaches (Supplemental Fig. 4A), accompanied by a slight up-regulation in transcription factor A mitochondrial (TFAM) protein levels (Fig. 4D), but no coordinate increase in full-length mtDNA genomes (7). We reasoned that this might indicate the presence of mtDNA instability in CLPP-deficient cells. In agreement with this hypothesis, we observed that CLPP-KO MEFs (Fig. 4A) and CLPP-depleted human fibroblasts (Supplemental Fig. 4B) displayed significant mtDNA nucleoid enlargement and aggregation by confocal microscopy. Indeed, quantification of nucleoids by confocal microscopy revealed markedly more mtDNA stress, as measured by a greater number of enlarged nucleoids (>450 nm² in area) in CLPP-KO MEFs compared with WT cells (Fig. 4B,



Supplemental Fig. 4D). These results are similar to the mtDNA stress phenotype observed in TFAM heterozygous (*Tfam*^{+/-}) MEFs, which have enlarged mtDNA nucleoids and mitochondrial network hyperfusion that result in the release and cytosolic accumulation of mtDNA, tonic cGAS–STING–IFN-I signaling, and antiviral priming (21).

mtDNA mediates IFN-I responses in CLPP-deficient fibroblasts

To next demonstrate that mtDNA is the DAMP triggering ISG responses in CLPP-KO MEFs, we treated cells with ddC, a nucleoside reverse transcriptase inhibitor that specifically inhibits mtDNA replication and causes robust mtDNA depletion with little effect on nuclear DNA (30). Notably, ddC treatment was sufficient to clear the enlarged/aggregated nucleoids in CLPP-KO MEFs (Fig. 4A, 4B), as well as robustly reduce mtDNA levels (Supplemental Fig. 4C) and nucleoid size (Supplemental Fig. 4D). Consistent with the notion that mtDNA stress is driving cGAS–STING–IFN-I signaling in CLPP-KO cells, the pronounced ISG signature observed in CLPP-KO MEFs was markedly reduced at the RNA and protein levels after ddC treatment (Fig. 4C, 4D).

In a complementary approach, we transfected MEFs with siRNA against *Polg2* to knock down the accessory subunit of the mtDNA polymerase pol γ that is required for mtDNA replication (31). Consistent with ddC results, we observed a significant reduction in ISG transcripts in CLPP-KO cells when *Polg2* was knocked down (Fig. 4E).

Recently, it was described that VBIT-4, an inhibitor of voltage-dependent anion channel (VDAC) oligomerization, blocks the formation of mitochondrial pores and prevents the release of mtDNA fragments into the cytosol of *Endog*-deficient MEFs (32). We next tested this reagent in our MEF lines, and similar to the results with ddC treatment and *Polg2* knockdown, VBIT-4 treatment significantly diminished the strong ISG signature of CLPP-KO MEFs at baseline (Fig. 4F). VBIT-4 had no effect on ISG expression induced by recombinant mouse IFN β treatment (Supplemental Fig. 4E), indicating that the abrogation of steady-state antiviral responses by VBIT-4 was not due to a general suppression of IFN-I signaling in CLPP-KO cells. Collectively, these results document that mtDNA stress and VDAC-mediated mtDNA released into the cytosol are key triggers of cGAS–STING–IFN-I signaling and antiviral responses in CLPP-KO cells.

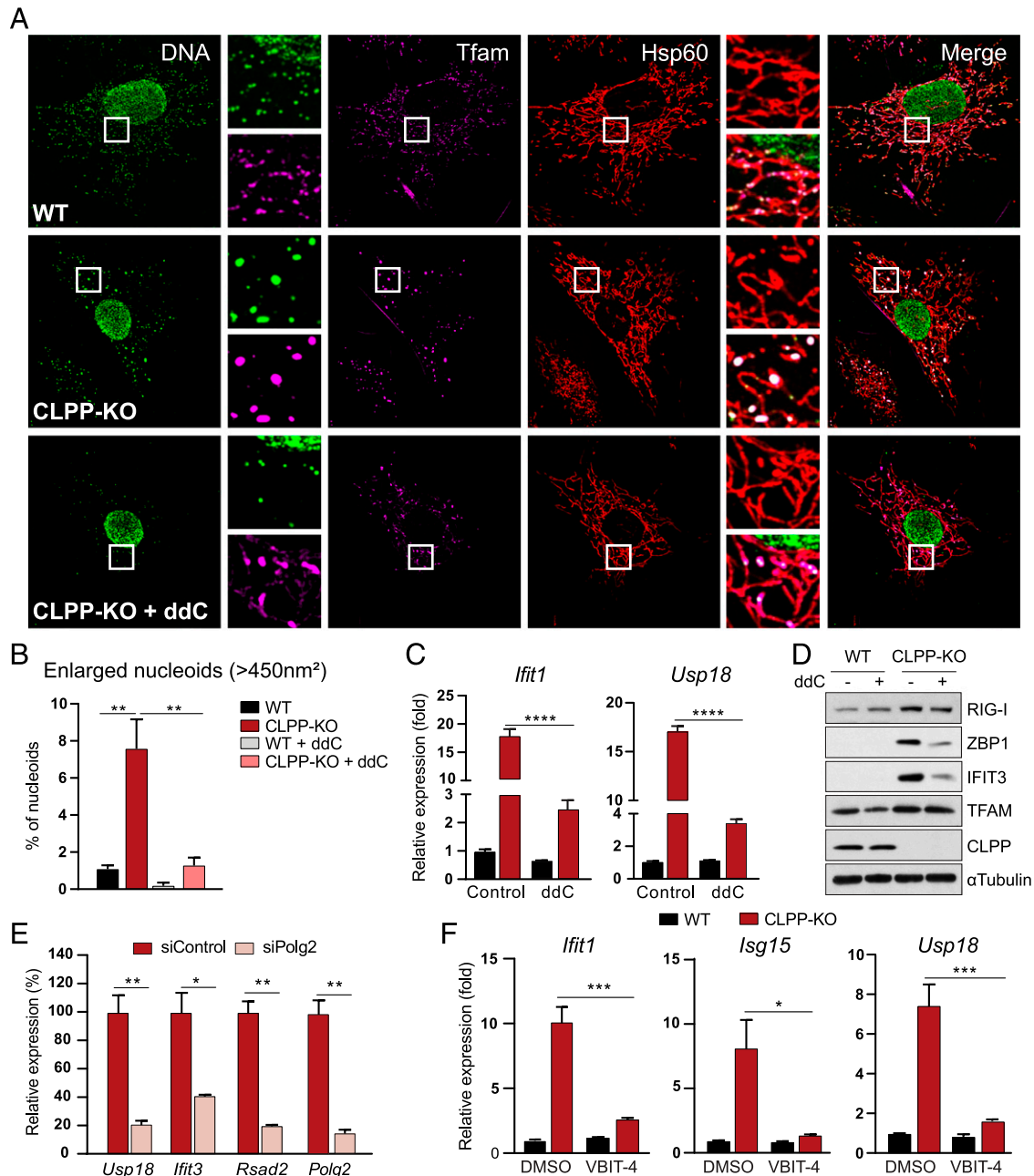


FIGURE 4. Altered mtDNA homeostasis mediates IFN-I responses in CLPP-KO fibroblasts. **(A–D)** WT and CLPP-KO MEFs were cultured in the presence of regular media (control) or media containing ddC (150 μ M). Cells were harvested after 4 d for **(A)** confocal microscopy with anti-DNA, anti-Tfam (mtDNA nucleoid marker), and anti-HSP60 (mitochondrial matrix protein). Images were collected with a 60 \times oil immersion objective, and white squares were digitally zoomed 5 \times . **(B)** Nucleoid quantification represented as percentage (%) of enlarged nucleoids (>450 nm²). **(C)** Quantitative real-time PCR analysis of ISG expression ($n = 3$ biological replicates). **(D)** Representative Western blots of ISG protein expression. **(E)** Quantitative real-time PCR of ISGs in CLPP-KO MEFs transfected with control or siPolg2 siRNA for 72 h ($n = 3$ biological replicates). **(F)** Quantitative real-time PCR of ISGs of WT and CLPP-KO MEFs treated with VBIT-4 (10 μ M) or control (DMSO) for 48 h ($n = 3$ biological replicates). In **(E)**, real-time PCR data are presented as relative expression percentage (%) setting control siRNA (siControl) as 100%. Error bars represent mean \pm SEM of triplicates, Student t test. In **(C)** and **(F)**, error bars represent mean \pm SEM of triplicates, two-way ANOVA Tukey post hoc. All experiments are representative of three to four independent experiments. * $p < 0.05$, ** $p < 0.01$, *** $p < 0.001$, **** $p < 0.0001$.

Finally, we explored other factors that modulate mtDNA stress and/or signaling to IFN-I to rule in or out their involvement in the enhanced ISG signature of CLPP-KO cells. Interestingly, CLPX, the chaperone and ATPase from the protease complex CLPXP, has been associated with maintenance of mtDNA nucleoids in human cells (33). Although CLPX is upregulated in CLPP-null cells, we found that siRNA knockdown of CLPX had no effect on nucleoid aggregation (data not shown) or steady-state ISG responses in CLPP-KO MEFs (Fig. 5A). We next employed siRNA approaches

to target both mitochondrial fusion and fission proteins because mitochondrial dynamics facilitate proper nucleoid distribution and removal of damaged mtDNA (34, 35). However, we found that transient downregulation of Mfn1 or the fission factor Drp1 did not significantly alter the ISG signature in CLPP-KO cells (Fig. 5B). Finally, to assess whether the ISG signature in CLPP-null cells is due to altered translation and/or accumulation of misfolded mtDNA-encoded proteins, we treated cells with CAM, a mitochondrial translation inhibitor, and measured ISG levels by

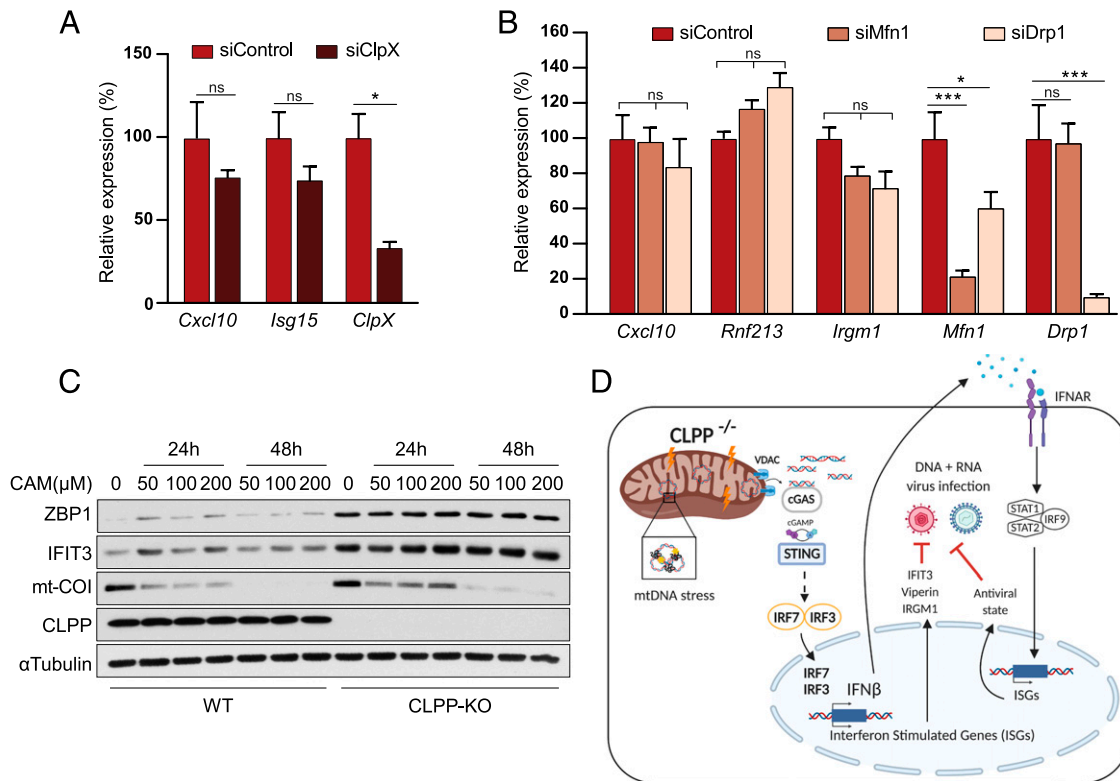


FIGURE 5. mtDNA stress-mediated IFN-I responses in CLPP-KO fibroblasts are independent of mitochondrial dynamics and translation. **(A and B)** Quantitative RT-PCR of ISGs in CLPP-KO MEFs transfected with siRNA control (Ctrl) and (A) siRNA against ClpX (siClpX) or (B) siRNA against Mfn1 (siMfn1) or Drp1 (siDrp1) for 72 h. Real-time PCR data are presented as relative expression percentage (%) considering CLPP-KO small interfering Ctrl (siControl) as 100% ($n = 3$ biological replicates). **(C)** Representative ISG protein levels of WT and CLPP-KO MEFs treated with CAM (50–200 μ M) over a 24–48-h time course. **(D)** Graphical abstract showing how absence of CLPP protease leads to mtDNA stress (packaging alterations), cytosolic release of mtDNA through VDAC pores, downstream signaling to the cGAS–STING–IFN-I axis, and broad viral resistance. Figure created with BioRender.com. Error bars represent mean \pm SEM of triplicates, and all experiments are representative of two to three independent experiments. In (A), Student t test was used, and in (B), a one-way ANOVA Tukey post hoc was used to determine significance. * $p < 0.05$, *** $p < 0.001$. ns, nonsignificant.

Western blotting after kinetic exposure. Exposures of low (50 μ M) to high (200 μ M) concentrations and durations of 24–48 h revealed that although CAM treatment robustly inhibited mitochondrial translation (as seen by significant reductions in mt-COI protein levels), it had no effect on the elevated steady-state ISG signature of CLPP-KO cells (Fig. 5C).

Discussion

ClpXP is an evolutionarily conserved, heteromeric, mitochondrial matrix localized serine protease complex, and despite extensive studies on prokaryotic ClpXP, the diverse functions of CLPXP in mitochondria remain less well defined (36). CLPP-null phenotypes in mice mirror human PS, displaying growth retardation, deafness, and premature sterility (10). Interestingly, CLPP-KO mice show immune alterations, with elevated expression of ISGs observed in peripheral tissues and fibroblasts (10, 18). However, the mitochondrial molecular mechanisms and innate immune signaling pathways underlying activation of antiviral signatures in CLPP-KO mice have not been defined, and the biological significance of immune alterations in CLPP-deficient cells and tissues has remained unclear.

Our results indicate that loss of CLPP in human and murine engages IFN-I responses via the cGAS–STING axis. Moreover, we have found that the primed IFN-I state of CLPP-KO cells is functionally relevant, conferring robust resistance to both RNA and DNA viruses (Fig. 5D). Similar viral resistance phenotypes have been reported in other cell lines with chronically activated IFN-I responses. Studies on cells lacking the exonuclease TREX1

or endoribonuclease RNaseH2, as well on *Tfam*^{+/-} MEFs, have revealed that baseline priming of IFN-I responses is sufficient to protect these cells from viral infection (21, 37–39). Similar to TREX1-, RNaseH2-, and TFAM-deficient cells, we have found that the viral resistance of CLPP-KO cells is mediated by baseline activation of the cGAS–STING pathway because protection against VSV and HSV-1 infection is lost in CLPP-KO/STING^{gt/gt} cells. The interesting finding that CLPP-KO/STING^{gt/gt} MEFs are more susceptible to HSV-1 infection may be due to the fact that HSV-1 is a robust modulator of host mitochondrial function and metabolism (40, 41). We hypothesize that the complete lack of cytosolic DNA sensing and antiviral IFN-I, combined with altered mitochondrial homeostasis in CLPP-KO/STING^{gt/gt} cells, likely synergize to increase HSV-1 virulence mechanisms and increase viral replication. Notably, HSV-1 can directly target host mtDNA through the virally encoded DNase UL12.5, resulting in nucleoid stress/enlargement, followed by rapid mtDNA depletion (21, 42, 43). Thus, increased interference with mtDNA homeostasis by UL12.5 or other encoded factors may potentially explain the elevated susceptibility of double-KO cells to HSV-1.

We have also found that loss of CLPP alters mtDNA homeostasis. Although more than 50 nucleoid-associated proteins have been shown to participate in mtDNA maintenance and gene expression, CLPP has not yet been implicated in either process (44). Our findings document that CLPP is necessary for maintaining mtDNA nucleoid organization and distribution, as CLPP-null cells exhibit markedly disrupted nucleoid architecture and TFAM aggregation compared with WT cells. Of note, a recent clinical study

revealed decreased *CLPP* mRNA levels and increased mtDNA abundance and in-patient fibroblasts harboring disease-associated *CLPP* mutations (45). Combined with our results in *CLPP*-deficient cells, these findings collectively suggest a conserved role for *CLPP* in regulation of mtDNA maintenance and a potential role for mtDNA stress in the pathogenesis of PS. However, our *CLPP* knockdown and KO fibroblasts do not exactly phenocopy patient cells harboring *CLPP* missense mutations associated with PS. These disease mutations are noted to alter key amino acids in a cluster near the docking site for *CLPX* interaction or in the active site of the peptidase (46). Future work to reintroduce synonymous pathogenic mutant *CLPP* proteins into *CLPP*-KO mice or to generate germline mutations in *Clpp* via CRISPR/Cas9 will help to determine how these disease relevant mutations contribute to mtDNA instability, IFN-I responses, and PS disease pathogenesis.

We found that treatment with ddC or siRNA against the pol γ accessory subunit, Polg2, to deplete mtDNA and aberrant nucleoids markedly reduced ISG responses of *CLPP*-KO cells. Moreover, blocking direct mtDNA release via VDAC was sufficient to ablate steady-state expression of ISGs in *CLPP*-KO MEFs. These results strongly indicate that mtDNA instability and escape into the cytosol are key upstream triggers of cGAS-STING-IFN-I signaling in cells lacking *CLPP*. It is also noteworthy that monoallelic loss of another matrix protease and mtDNA maintenance factor, LONP1, leads to steady-state induction of ISGs in MEFs (18). This indicates that perturbations in mitochondrial matrix protease levels, which disrupt mtDNA homeostasis and stability, generally engage IFN-I signaling, thus linking mammalian UPR^{mt} factors to antiviral innate immunity (5, 47, 48). In addition, another study identified ERAL1, a putative 12S rRNA chaperone, as a *CLPX* substrate, implicating *CLPP* in mitoribosomal assembly and mitochondrial translation (7). Although mitoribosomal maturation/assembly was not analyzed carefully in this study, treatment with CAM to inhibit mitochondrial translation did not bring down steady-state IFN-I responses or lessen the aberrant nucleoid morphology in *CLPP*-KO cells (data not shown). Future studies aimed at uncovering the molecular mechanisms by which *CLPP* integrates mitoribosomal assembly, proteostasis, mitochondrial nucleoid organization, and mtDNA release should yield new insight into cross-talk between the mammalian UPR^{mt} and the innate immune system.

CLPP-KO mice exhibit reduced adiposity, increased whole-body energy expenditure, and protection from diet-induced obesity, indicating a role of *CLPP* in metabolic rewiring (12). Although deletion of *STING* or *IFNAR* ablated the ISG signature in *CLPP*-KO tissues, loss of either protein in vivo was not sufficient to rescue the small body size of *CLPP*-KO mice. Moreover, body composition analysis revealed that deletion of *STING* did not rescue the decreased fat/increased lean mass observed in *CLPP*-KO mice. Although our study does not directly address the role of *STING*-IFN-I signaling in infertility or deafness in *CLPP*-KO mice, we did find that the small testis size observed in *CLPP*-KO mice was not rescued by ablation of *STING* or *IFNAR*. However, several studies have linked IFN-I to sterility in both transgenic mouse models and human patients receiving exogenous IFN- α therapy (49–51). Moreover, sudden hearing loss has been reported as an adverse effect of IFN- α immunotherapy in patients with hepatitis C virus or cancer (52, 53). Therefore, it will be interesting to more carefully explore whether ablation of *STING* or *IFNAR* in *CLPP*-KO mice impacts the development or progression of sterility and/or deafness, which may have implications for understanding the role of *STING*-IFN-I signaling in the diverse pathology of human PS.

In conclusion, our results place the cGAS-STING-IFN-I innate immune pathway downstream of *CLPP* and illuminate links between mitochondrial proteostasis, mtDNA genome maintenance, and antiviral immunity. Imbalances in mitochondrial protease function, mtDNA damage, and innate immunity are each associated with various pathological conditions, such as neurodegenerative disorders, infertility, metabolic syndromes, and cancer (36, 54). Our work therefore sheds light on the biology of mammalian *CLPP*, further advances our understanding of mitochondrial-innate immune cross-talk, and may have implications for understanding PS pathogenesis and other diseases involving *CLPP* dysregulation.

Acknowledgments

We thank our colleagues in the West Lab for feedback on the manuscript, as well as Dr. Malea Murphy in the Integrated Microscopy and Imaging Laboratory at the Texas A&M College of Medicine for assistance with confocal imaging.

Disclosures

The authors have no financial conflicts of interest.

References

- Quirós, P. M., T. Langer, and C. López-Otín. 2015. New roles for mitochondrial proteases in health, ageing and disease. *Nat. Rev. Mol. Cell Biol.* 16: 345–359.
- Baker, T. A., and R. T. Sauer. 2012. ClpXP, an ATP-powered unfolding and protein-degradation machine. *Biochim. Biophys. Acta* 1823: 15–28.
- Bhandari, V., K. S. Wong, J. L. Zhou, M. F. Mabanglo, R. A. Batey, and W. A. Houry. 2018. The role of ClpP protease in bacterial pathogenesis and human diseases. *ACS Chem. Biol.* 13: 1413–1425.
- Haynes, C. M., K. Petrova, C. Benedetti, Y. Yang, and D. Ron. 2007. ClpP mediates activation of a mitochondrial unfolded protein response in *C. elegans*. *Dev. Cell* 13: 467–480.
- Pellegrino, M. W., A. M. Nargund, N. V. Kirienko, R. Gillis, C. J. Fiorese, and C. M. Haynes. 2014. Mitochondrial UPR-regulated innate immunity provides resistance to pathogen infection. *Nature* 516: 414–417.
- Deepa, S. S., S. Bhaskaran, R. Ranjit, R. Qaisar, B. C. Nair, Y. Liu, M. E. Walsh, W. C. Fok, and H. Van Remmen. 2016. Down-regulation of the mitochondrial matrix peptidase ClpP in muscle cells causes mitochondrial dysfunction and decreases cell proliferation. *Free Radic. Biol. Med.* 91: 281–292.
- Szczepanowska, K., P. Maiti, A. Kukat, E. Hofsetz, H. Nolte, K. Senft, C. Becker, B. Ruzzenente, H.-T. Hornig-Do, R. Wibom, et al. 2016. *CLPP* coordinates mitoribosomal assembly through the regulation of ERAL1 levels. *EMBO J.* 35: 2566–2583.
- Ishizawa, J., S. F. Zarabi, R. E. Davis, O. Halgas, T. Nii, Y. Jitkova, R. Zhao, J. St-Germain, L. E. Heese, G. Egan, et al. 2019. Mitochondrial ClpP-mediated proteolysis induces selective cancer cell lethality. *Cancer Cell* 35: 721–737.e9.
- Graves, P. R., L. J. Aponte-Collazo, E. M. J. Fennell, A. C. Graves, A. E. Hale, N. Dicheva, L. E. Herring, T. S. K. Gilbert, M. P. East, I. M. McDonald, et al. 2019. Mitochondrial protease ClpP is a target for the anticancer compounds ONC201 and related analogues. *ACS Chem. Biol.* 14: 1020–1029.
- Gispert, S., D. Parganlija, M. Klinkenberg, S. Dröse, I. Wittig, M. Mittelbronn, P. Grzmil, S. Koob, A. Hamann, M. Walter, et al. 2013. Loss of mitochondrial peptidase ClpP leads to infertility, hearing loss plus growth retardation via accumulation of *CLPX*, mtDNA and inflammatory factors. *Hum. Mol. Genet.* 22: 4871–4887.
- Jenkinson, E. M., A. U. Rehman, T. Walsh, J. Clayton-Smith, K. Lee, R. J. Morell, M. C. Drummond, S. N. Khan, M. A. Naeem, B. Rauf, et al; University of Washington Center for Mendelian Genomics. 2013. Perrault syndrome is caused by recessive mutations in *CLPP*, encoding a mitochondrial ATP-dependent chambered protease. *Am. J. Hum. Genet.* 92: 605–613.
- Bhaskaran, S., G. Pharaoh, R. Ranjit, A. Murphy, S. Matsuzaki, B. C. Nair, B. Forbes, S. Gispert, G. Auburger, K. M. Humphries, et al. 2018. Loss of mitochondrial protease ClpP protects mice from diet-induced obesity and insulin resistance. *EMBO Rep.* 19: e45009.
- Wang, T., E. Babayev, Z. Jiang, G. Li, M. Zhang, E. Esencan, T. Horvath, and E. Seli. 2018. Mitochondrial unfolded protein response gene *Clpp* is required to maintain ovarian follicular reserve during aging, for oocyte competence, and development of pre-implantation embryos. *Aging Cell* 17: e12784.
- Becker, C., A. Kukat, K. Szczepanowska, S. Hermans, K. Senft, C. P. Brandscheid, P. Maiti, and A. Trifunovic. 2018. *CLPP* deficiency protects against metabolic syndrome but hinders adaptive thermogenesis. *EMBO Rep.* 19: e45126.
- West, A. P., and G. S. Shadel. 2017. Mitochondrial DNA in innate immune responses and inflammatory pathology. *Nat. Rev. Immunol.* 17: 363–375.
- Nakahira, K., S. Hisata, and A. M. K. Choi. 2015. The roles of mitochondrial damage-associated molecular patterns in diseases. *Antioxid. Redox Signal.* 23: 1329–1350.
- Youle, R. J. 2019. Mitochondria-Striking a balance between host and endosymbiont. *Science* 365: eaaw9855.

18. Key, J., A. Maletzko, A. Kohli, S. Gispert, S. Torres-Odio, I. Wittig, J. Heidler, C. Bárcena, C. López-Otín, Y. Lei, et al. 2020. Loss of mitochondrial ClpP, Lonp1, and Tfam triggers transcriptional induction of Rnf213, a susceptibility factor for moyamoya disease. *Neurogenetics* 21: 187–203.
19. Dalton, K. P., and J. K. Rose. 2001. Vesicular stomatitis virus glycoprotein containing the entire green fluorescent protein on its cytoplasmic domain is incorporated efficiently into virus particles. *Virology* 279: 414–421.
20. Desai, P., and S. Person. 1998. Incorporation of the green fluorescent protein into the herpes simplex virus type 1 capsid. *J. Virol.* 72: 7563–7568.
21. West, A. P., W. Khoury-Hanold, M. Staron, M. C. Tal, C. M. Pineda, S. M. Lang, M. Bestwick, B. A. Duguay, N. Raimundo, D. A. MacDuff, et al. 2015. Mitochondrial DNA stress primes the antiviral innate immune response. *Nature* 520: 553–557.
22. Key, J., A. Kohli, C. Bárcena, C. López-Otín, J. Heidler, I. Wittig, and G. Auburger. 2019. Global proteome of *LonP1*^{+/−} mouse embryonal fibroblasts reveals impact on respiratory chain, but no interdependence between Ernl1 and mitoribosomes. *Int. J. Mol. Sci.* 20: 4523.
23. Cox, J., and M. Mann. 2008. MaxQuant enables high peptide identification rates, individualized p.p.b.-range mass accuracies and proteome-wide protein quantification. *Nat. Biotechnol.* 26: 1367–1372.
24. Volkman, H. E., S. Cambier, E. E. Gray, and D. B. Stetson. 2019. Tight nuclear tethering of cGAS is essential for preventing autoreactivity. *Elife* 8: e47491.
25. Rongvaux, A., R. Jackson, C. C. D. Harman, T. Li, A. P. West, M. R. de Zoete, Y. Wu, B. Yordy, S. A. Lakhani, C.-Y. Kuan, et al. 2014. Apoptotic caspases prevent the induction of type I interferons by mitochondrial DNA. *Cell* 159: 1563–1577.
26. Dhir, A., S. Dhir, L. S. Borowski, L. Jimenez, M. Teitell, A. Rötig, Y. J. Crow, G. I. Rice, D. Duffy, C. Tamby, et al. 2018. Mitochondrial double-stranded RNA triggers antiviral signalling in humans. *Nature* 560: 238–242.
27. Franz, K. M., W. J. Neidermyer, Y.-J. Tan, S. P. J. Whelan, and J. C. Kagan. 2018. STING-dependent translation inhibition restricts RNA virus replication. *Proc. Natl. Acad. Sci. USA* 115: E2058–E2067.
28. Ahn, J., and G. N. Barber. 2019. STING signaling and host defense against microbial infection. *Exp. Mol. Med.* 51: 1–10.
29. Zevini, A., D. OLAGNIE, and J. Hiscott. 2017. Crosstalk between cytoplasmic RIG-I and STING sensing pathways. *Trends Immunol.* 38: 194–205.
30. Kasashima, K., M. Sumitani, and H. Endo. 2011. Human mitochondrial transcription factor A is required for the segregation of mitochondrial DNA in cultured cells. *Exp. Cell Res.* 317: 210–220.
31. Young, M. J., and W. C. Copeland. 2016. Human mitochondrial DNA replication machinery and disease. *Curr. Opin. Genet. Dev.* 38: 52–62.
32. Kim, J., R. Gupta, L. P. Blanco, S. Yang, A. Shteinfein-Kuzmine, K. Wang, J. Zhu, H. E. Yoon, X. Wang, M. Kerkhofs, et al. 2019. VDAC oligomers form mitochondrial pores to release mtDNA fragments and promote lupus-like disease. *Science* 366: 1531–1536.
33. Kasashima, K., M. Sumitani, and H. Endo. 2012. Maintenance of mitochondrial genome distribution by mitochondrial AAA+ protein ClpX. *Exp. Cell Res.* 318: 2335–2343.
34. Ban-Ishihara, R., T. Ishihara, N. Sasaki, K. Mihara, and N. Ishihara. 2013. Dynamics of nucleoid structure regulated by mitochondrial fission contributes to cristae reformation and release of cytochrome c. *Proc. Natl. Acad. Sci. USA* 110: 11863–11868.
35. Malena, A., E. Loro, M. Di Re, I. J. Holt, and L. Vergani. 2009. Inhibition of mitochondrial fission favours mutant over wild-type mitochondrial DNA. *Hum. Mol. Genet.* 18: 3407–3416.
36. Levyttsky, R. M., E. M. Germany, and O. Khalimonchuk. 2016. Mitochondrial quality control proteases in neuronal welfare. *J. Neuroimmune Pharmacol.* 11: 629–644.
37. Hasan, M., V. K. Gonugunta, N. Dobbs, A. Ali, G. Palchik, M. A. Calvaruso, R. J. DeBerardinis, and N. Yan. 2017. Chronic innate immune activation of TBK1 suppresses mTORC1 activity and dysregulates cellular metabolism. *Proc. Natl. Acad. Sci. USA* 114: 746–751.
38. Schoggins, J. W., S. J. Wilson, M. Panis, M. Y. Murphy, C. T. Jones, P. Bieniasz, and C. M. Rice. 2011. A diverse range of gene products are effectors of the type I interferon antiviral response. [Published erratum appears in 2015 *Nature* 525: 144.] *Nature* 472: 481–485.
39. Pokatayev, V., N. Hasin, H. Chon, S. M. Cerritelli, K. Sakhuja, J. M. Ward, H. D. Morris, N. Yan, and R. J. Crouch. 2016. RNase H2 catalytic core Aicardi-Goutières syndrome-related mutant invokes cGAS-STING innate immune-sensing pathway in mice. *J. Exp. Med.* 213: 329–336.
40. Duarte, L. F., M. A. Farias, D. M. Alvarez, S. M. Bueno, C. A. Riedel, and P. A. González. 2019. Herpes simplex virus type 1 infection of the central nervous system: insights into proposed interrelationships with neurodegenerative disorders. *Front. Cell. Neurosci.* 13: 46.
41. Reshi, L., H.-V. Wang, and J.-R. Hong. 2018. Modulation of mitochondria during viral infections. In *Mitochondrial Diseases*. E. Taskin, C. Guven, and Y. Sevgiler, eds. IntechOpen, London. DOI: 10.5772/intechopen.73036.
42. Saffran, H. A., J. M. Pare, J. A. Corcoran, S. K. Weller, and J. R. Smiley. 2007. Herpes simplex virus eliminates host mitochondrial DNA. *EMBO Rep.* 8: 188–193.
43. Corcoran, J. A., H. A. Saffran, B. A. Duguay, and J. R. Smiley. 2009. Herpes simplex virus UL12.5 targets mitochondria through a mitochondrial localization sequence proximal to the N terminus. *J. Virol.* 83: 2601–2610.
44. Lee, S. R., and J. Han. 2017. Mitochondrial nucleoid: shield and switch of the mitochondrial genome. *Oxid. Med. Cell. Longev.* DOI: doi.org/10.1155/2017/8060949.
45. Theunissen, T. E. J., R. Szklarczyk, M. Gerards, D. M. E. I. Hellebrekers, E. N. M. Mulder-Den Hartog, J. Vanoevelen, R. Kamps, B. de Koning, S. L. Rutledge, T. Schmitt-Mechelke, et al. 2016. Specific MRI abnormalities reveal severe Perrault syndrome due to CLPP defects. *Front. Neurol.* 7: 203.
46. Brodie, E. J., H. Zhan, T. Saiyed, K. N. Truscott, and D. A. Dougan. 2018. Perrault syndrome type 3 caused by diverse molecular defects in CLPP. *Sci. Rep.* 8: 12862.
47. Wang, S., K. Gao, and Y. Liu. 2018. UPR^{mt} coordinates immunity to maintain mitochondrial homeostasis and animal fitness. *Mitochondrion* 41: 9–13.
48. Melber, A., and C. M. Haynes. 2018. UPR^{mt} regulation and output: a stress response mediated by mitochondrial-nuclear communication. *Cell Res.* 28: 281–295.
49. Ulusoy, E., S. Çayan, N. Yılmaz, S. Aktaş, D. Acar, and E. Doruk. 2004. Interferon alpha-2b may impair testicular histology including spermatogenesis in a rat model. *Arch. Androl.* 50: 379–385.
50. Hekman, A. C., J. Trapman, A. H. Mulder, J. L. van Gaalen, and E. C. Zwarthoff. 1988. Interferon expression in the testes of transgenic mice leads to sterility. *J. Biol. Chem.* 263: 12151–12155.
51. Iwakura, Y., M. Asano, Y. Nishimune, and Y. Kawade. 1988. Male sterility of transgenic mice carrying exogenous mouse interferon β gene under the control of the metallothionein enhancer-promoter. *EMBO J.* 7: 3757–3762.
52. Asal, S., O. Sobhy, O. Ismail, and E. Bedewy. 2014. Study of the effect of combined interferon and ribavirin therapy on the hearing profile of hepatitis C virus patients. *Egypt. J. Otolaryngol.* 31: 237–243.
53. Formann, E., R. Stauber, D.-M. Denk, W. Jessner, G. Zollner, P. Munda-Steindl, A. Gangl, and P. Ferenci. 2004. Sudden hearing loss in patients with chronic hepatitis C treated with pegylated interferon/ribavirin. *Am. J. Gastroenterol.* 99: 873–877.
54. Barcena, C., P. Mayoral, P. Quiros, and C. Lopez-Otin. 2017. Physiological and pathological functions of mitochondrial proteases. In *Proteases in Physiology and Pathology*. S. Chakraborti, and N. Dhalla, eds. Springer, Singapore, p. 3–25.

GSE Accession number: GSE40207
Microarray Profiling

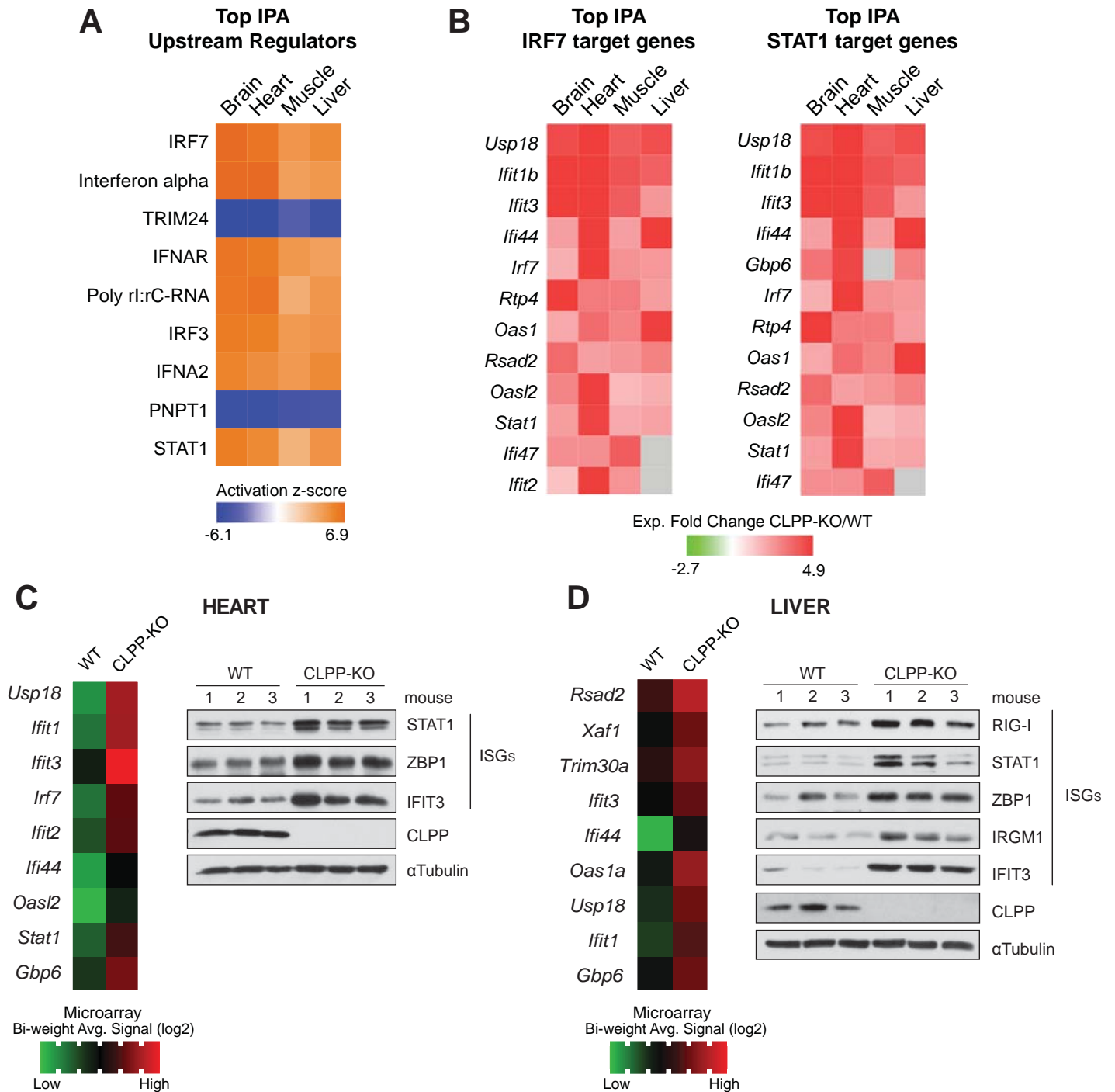


Figure S1. CLPP-KO mice exhibit elevated ISG RNA and protein abundance in brain, heart, muscle and liver. (A, B) Microarray profiling from results reported in Gispert S et al, 2013, GEO Accession GSE40207. Heatmaps of Ingenuity Pathway Analysis (IPA) predicted upstream regulators (A) and putative IRF7 and STAT1 target genes of the antiviral gene signature (B) in CLPP-KO brain, heart, muscle and liver tissues (n=3 mice). (C-D) Heatmaps showing most significantly upregulated ISGs from microarray data (GSE40207). Western blots of baseline ISGs in heart (C) and liver (D) tissues of WT and CLPP-KO male mice, between 3-5 months old. Numbers 1, 2, and 3 indicate a different mouse.

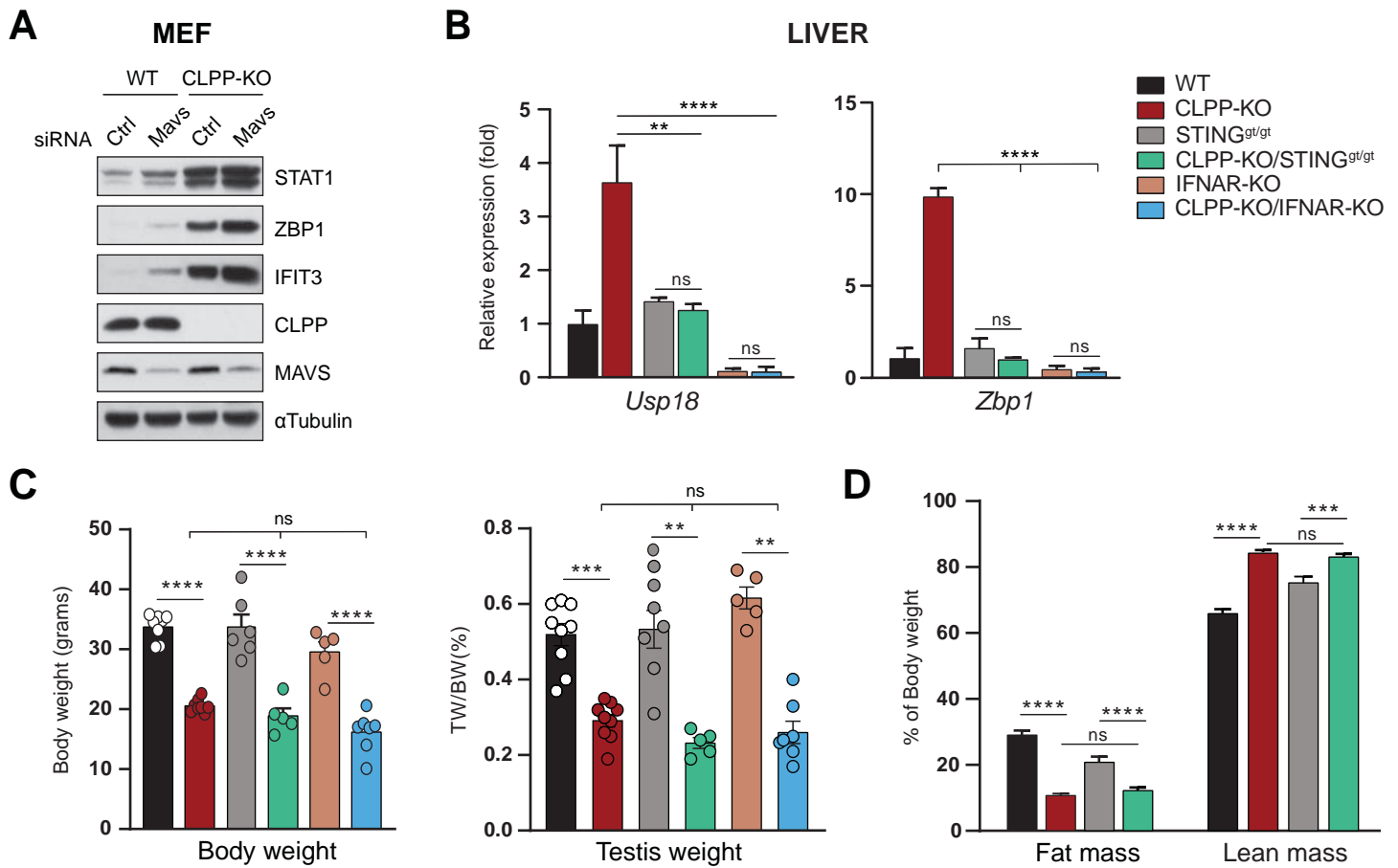


Figure S2. STING and IFNAR signaling drive elevated ISG responses in CLPP deficient cells and tissues, but ablation of IFN-I signaling does not lessen growth retardation of CLPP KO mice. (A) Western blots of ISGs of WT and CLPP-KO MEFs transfected with siRNA Control (Ctrl) and siMavs for 72hrs. (B) Quantitative real-time PCR of baseline ISGs of liver tissue from 12-month old male mice. (C) Body weight (BW) and testis weight (TW, normalized to body weight: TW/BW) analysis of 5-7-month old male mice from 6 different genotypes ($n= 5-8$ mice). (D) Fat mass and lean mass measurements in 7-10-month old female WT, CLPP-KO, STING^{gt/gt} and CLPP-KO/STING^{gt/gt} mice, as assessed by EchoMRI and normalized to body weight ($n= 6-10$ mice). In B, data are presented as mean \pm s.e.m. of triplicate technical replicates from $n=3$ mice. In (B, C) $**p<0.01$, $****p<0.0001$, ns non-significant (One-way ANOVA Tukey's post-hoc). In (D), $***p<0.001$, $****p<0.0001$, ns non-significant (Two-way ANOVA Tukey's post-hoc).

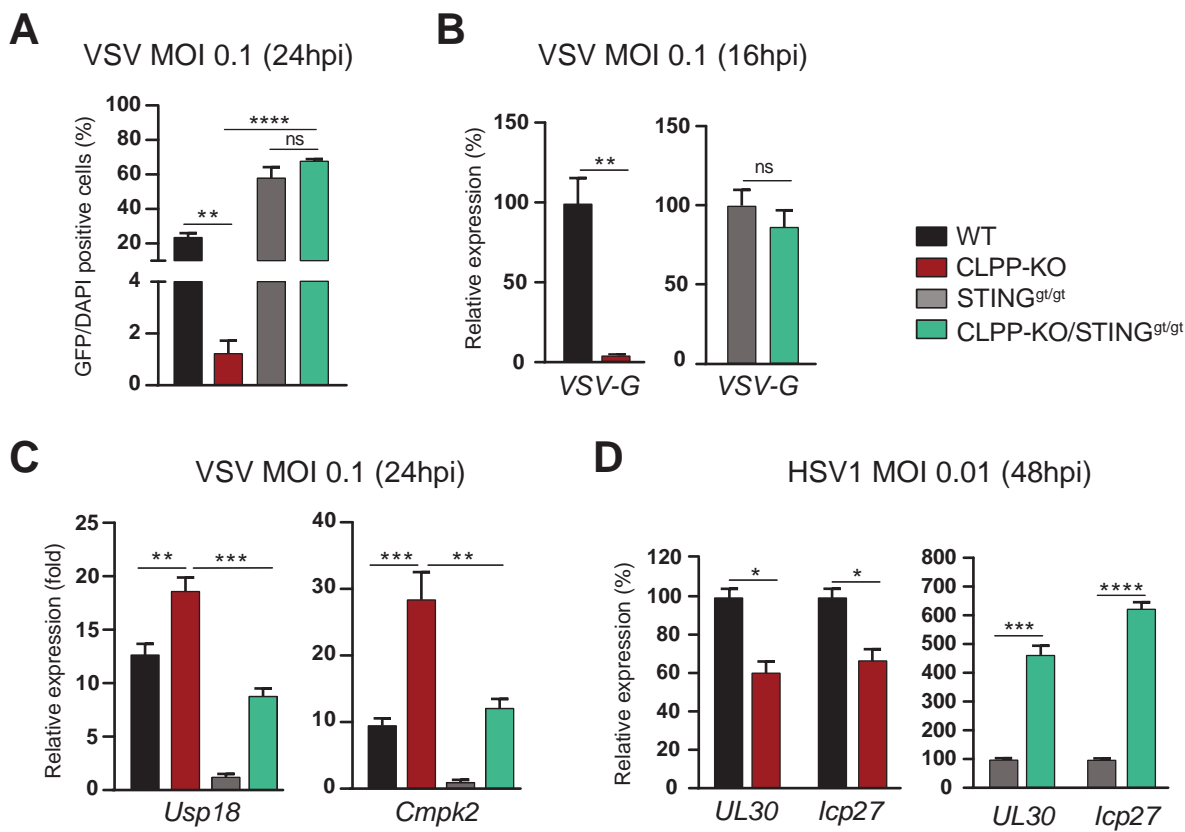


Figure S3. CLPP-KO fibroblasts are more resistant to viral infection owing to elevated activation of the STING pathway. (A) Quantification of GFP staining in MEFs at MOI 0.1 24hrs after VSV infection. Data represented as percentage of GFP/DAPI positive cells. (B) Quantitative real-time PCR of viral RNA at MOI 0.1 16hrs after VSV infection. (C) Quantitative real-time PCR of ISGs 24hrs after VSV infection at MOI of 0.1. (D) Quantitative real-time PCR of viral RNA in MEFs infected with HSV-1 at 48hpi and MOI of 0.01. In (B, D) Real-time RT-PCR data are presented as relative expression percentage (%) comparing CLPP-KO vs WT and CLPP-KO/STING^{g^t/g^t} vs STING^{g^t/g^t} MEFs. Error bars indicate \pm s.e.m. of triplicate biological replicates (Student's t-test). In C, data are presented as mean \pm s.e.m. of triplicate biological replicates (One-way ANOVA Tukey's post hoc). * $p < 0.05$, ** $p < 0.01$, *** $p < 0.001$, **** $p < 0.0001$, ns non-significant.

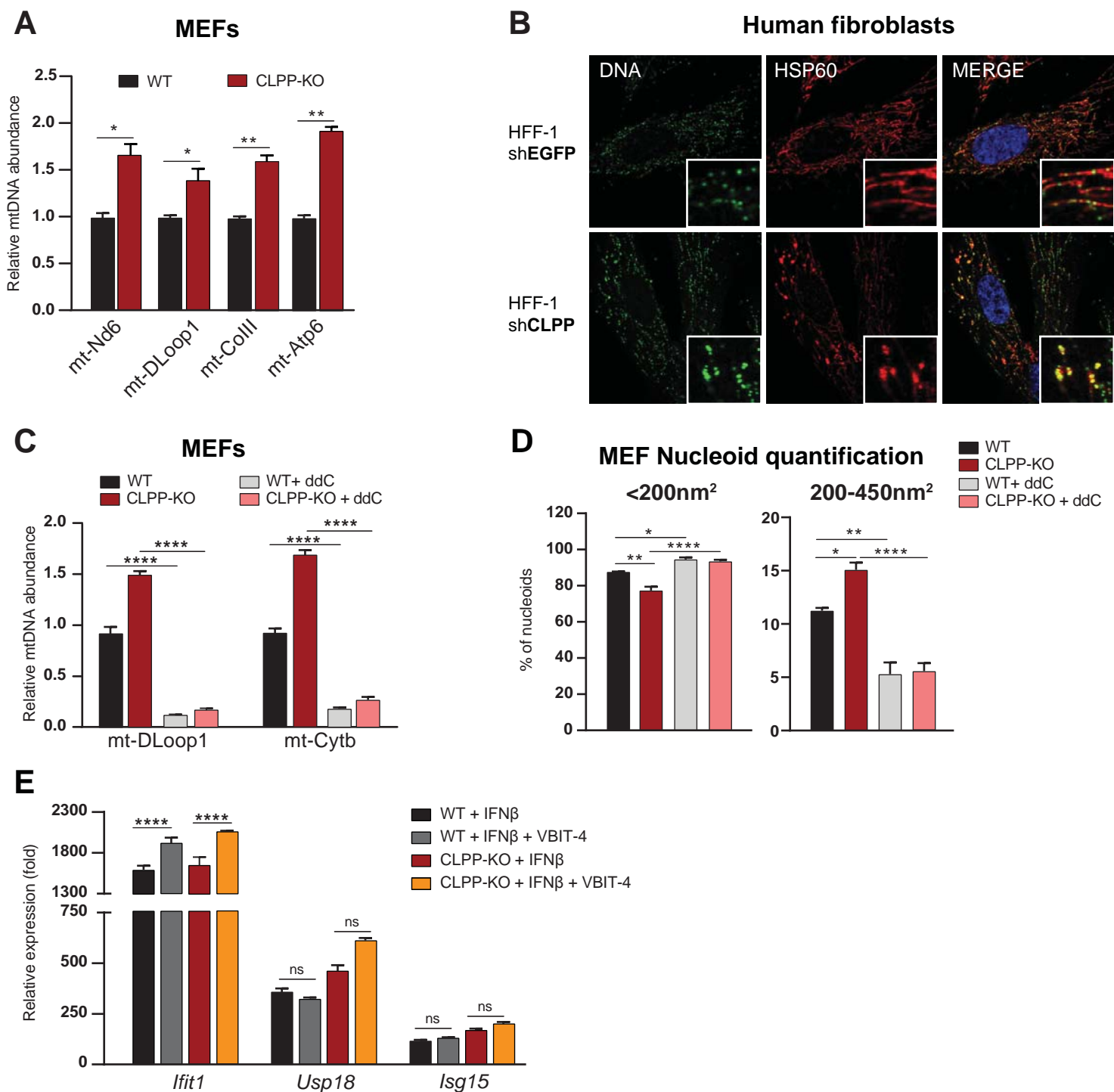


Figure S4. Altered mtDNA homeostasis mediates IFN-I responses in mouse and human CLPP deficient fibroblasts. (A) Quantification of mtDNA abundance relative to nuclear DNA (*Tert*) in WT and CLPP-KO MEFs at baseline (n=3 MEF lines). (B) Human foreskin fibroblasts (HFF-1) were transduced with the shRNA encoding CLPP and EGFP (as control) and selected with puromycin (2 μ g/ml). After selection, cells were plated in 12-well dishes, fixed, and stained with anti-DNA (DNA), anti-HSP60 (mitochondria) and DAPI before imaging on a confocal microscope with a 60X oil immersion objective (n=1 line). (C) Quantification of mtDNA abundance relative to nuclear DNA (*Tert*) in WT and CLPP-KO MEF before and after ddC treatment (n=3 lines). (D) Quantification of nucleoid size in control and ddC-treated WT and CLPP-KO MEFs. Data represented as percentage of nucleoids in each size range: <200nm² or 200-450nm² (n=2 lines). (E) Quantitative real time PCR of ISGs of WT and CLPP-KO MEFs treated with VBIT-4 (10 μ M) and challenged with mIFN β (1 ng/ml) for 6hrs (n=2 lines). In (A, C) data are presented as mean \pm s.e.m. of biological replicates (Student's t-test). In E, data are presented as mean \pm s.e.m. of triplicate biological replicates (Two-way ANOVA Tukey's post hoc). *p<0.05, **p<0.01, ***p<0.001, ****p<0.0001.